Max-Planck-Institut
für Quantenoptik
BIBLIOTHEK
D-8046 Garchi

Handbibliothek
MPQ

[redacted]

MPQ-Report
48

MPQ

MAX-PLANCK-INSTITUT FÜR QUANTENOPTIK

8046 GARCHING BEI MÜNCHEN

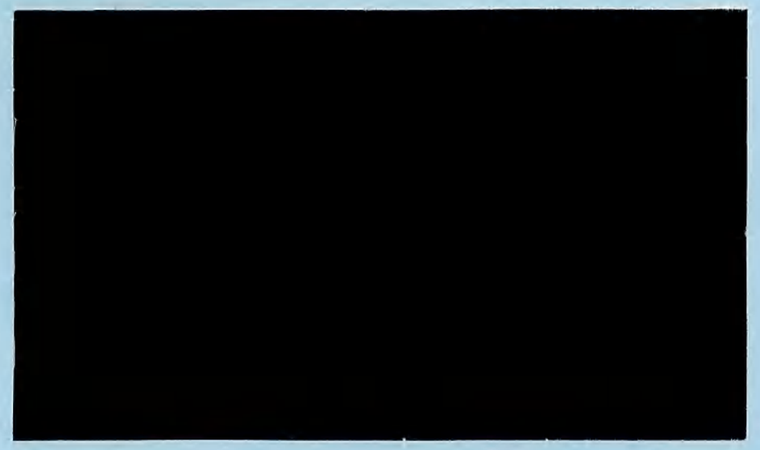

MAX-PLANCK-INSTITUT FÜR QUANTENOPTIK

Target Design for Heavy Ion Beam Fusion

J. Meyer-ter-Vehn and N. Metzler

MPQ 48 July 1981

Max-Planck-Institut
für Quantenoptik
BIBLIOTHEK
D-8046 Garching

Diese Arbeit wurde gefördert vom Bundesministerium
für Forschung und Technologie

D-8046 Garching bei München

MPQ 48 / 1981

Target Design for Heavy Ion Beam Fusion

J. Meyer-ter-Vehn and N. Metzler

July 1981

Abstract

Target design for Heavy Ion Beam Fusion and related physics are discussed. First, a modified version of the Kidder-Bodner model for pellet gain is presented and is used to define the working point (E_{Beam} = 4.8 MJ, Gain 83) for a reactor size target. Secondly, stopping of heavy ions in hot dense plasma is investigated and numerical results for stopping powers and ranges of 10 GeV Bi-ions in Pb, Li, and PbLi-alloy are given. Finally, results of an explicit implosion calculation, using the 1-D code MINIHY, are discussed in detail. The hydrodynamic efficiency is found to be about 5 %. Special attention is given to the shock sequence leading to the ignition configuration. Also the growth of Rayleigh-Taylor instability at the absorber-pusher interface is estimated.

Table of contents

1. Introduction

2. Modified Kidder-Bodner model for pellet gain

3. Heavy ion stopping powers in hot dense plasma
   3.1 General considerations
   3.2 The theoretical model
   3.3 Calculated ranges and stopping powers

4. A specific pellet design
   4.1 General considerations
   4.2 The pellet configuration
   4.3 The pellet code MINIHY
   4.4 The pellet implosion
      4.4.1 The general view
      4.4.2 Absorber, pusher, and fuel during implosion
      4.4.3 Ignition and burn
      4.4.4 Pulse shape, shocks, ignition
      4.4.5 Estimated growth of Rayleigh-Taylor instability

5. Conclusions

1. Introduction

The work on target design for Heavy Ion Beam Fusion (HIF) which is presented here is part of the FRG program to investigate the use of heavy ion beams for inertial confinement fusion (ICF). It has been performed in connection with the HIBALL reactor design study and will be included in the HIBALL report*). It is a first step within the FRG program to study ICF target behaviour and related physics.

Heavy ion beams have been considered as promising drivers for ICF mainly because of the following reasons:

1. high driver efficiency (≈ 25 %)
2. classical beam transport
3. efficient energy deposition on target

Due to the high stopping powers, the range of 10 GeV heavy ions in solid matter amounts to less than 1 mm. This allows for relatively low beam currents in the order of 10 kA in order to achieve the beam powers (some 100 TW) required for ICF. It is assumed that the total beam is split up in a number of individual beams which are then focused on the small target sphere (pellet) in a spherically symmetric way. The present work deals with the physics and dynamics of the pellet implosion including beam deposition, core compression and fuel ignition.

ICF applications have stirred up new interest to study ion stopping in hot dense matter. The relevant regime is characterized by solid densities, temperatures up to 1 keV and non-relativistic ion energies up to 100 MeV/nucleon. In case of heavy ions, an important quantity is the average charge of the ion inside the stopping medium. There exists no experimental information for stopping powers in this regime. On the theory side, generalisation of standard stopping models to hot dense matter is straightforward as outlined in the present work and used to calculate ranges and deposition pro-

*) HIBALL, Conceptual Heavy Ion Beam Fusion Reactor Design Study, Report Kernforschung Karlsruhe / FRG, to appear in 1981.

files. There remain questions, however, concerning the validity of the approach, and a more rigorous theoretical treatment of this problem should be worked out in the future.

The target is the key element of inertial confinement fusion. A high energy gain of the target (fusion energy / input beam energy $\approx$ 100) is required for power reactor applications. The feasibility of high gain targets is infered from theoretical analysis and simulation, but is has not yet been demonstrated in experiments. In the following, gain curves (gain vs. input energy) have been calculated as a function of a few physical parameters within a simple model (modified Kidder-Bodner model). Typical values for these parameters in the case of heavy ion beam fusion are then obtained from an explicit implosion calculation using the 1D-hydrodynamic code MINIHY. Results of this calculation are discussed in detail, providing insight into the evolution of pressure, density and temperature patterns of a typical HIF pellet implosion. Also the shock sequence leading to fuel ignition is analysed.

It should be noted that no HIF target designs for reactor applications have been reported in the journal literature, so far. The general configuration of the present design has been adapted from a light ion beam target reported by Bangerter and Meeker. It is a single hollow shell target with three layers including cryogenic DT. Changes in size and material have been chosen to meet with global parameters of the HIBALL reactor design to which the present work is related. Some relevant HIBALL parameters are listed below:

HIBALL parameters	
Ion	Bi^{2+}
Ion energy	10 GeV
Beam energy	4.8 MJ
Max. beam power	240 TW
Beam focus radius	3 mm
Target materials	Pb-Li-DT
Target yield	400 MJ
Target gain	83

More information is given in the HIBALL report.

A most critical issue in ICF target performance is the spherical symmetry of the implosion. It is intimately connected with the problem of igniting a small portion of the DT fuel (spark). Starting typically with a specific energy deposition of 20-40 MJ/g in the beam absorbing regions, spherical convergence is crucial to achieve an energy concentration of more than 500 MJ/g in the spark necessary for ignition. Both asymmetries in beam irradiation and fluid instabilities may destroy the spherical symmetry during implosion. With respect to ion beam fusion, this point appears to be particularly dangerous. Since the beam deposits energy into dense material at relatively low temperature, heat conduction is rather inefficient to smooth out asymmetries. In the present work, based on 1D simulation, we are not in a state to assess the symmetry issue adequately. However, its importance is pointed out, and an estimate for Rayleigh-Taylor growth is given.

1. Modified Kidder-Bodner model for pellet gain

Pellet gain as a function of beam energy is one of the crucial relations for inertial confinement fusion. Although the dynamics of pellet implosion are very complex, the gain curve can be expressed in terms of a few physical parameters. This has recently been pointed out by S. Bodner.[1] The underlying model had been formulated before by R. Kidder [2]. The fuel configuration at ignition is assumed to consist of a central hot region (spark) surrounded by highly compressed fuel at low entropy as shown schematically in fig. 1. Ignition will occur in the centre, and burn then propagates into the cold fuel. Propagating burn is essential to achieve high gain. The question of how to achieve such an ignition configuration dynamically is addressed in section 3.

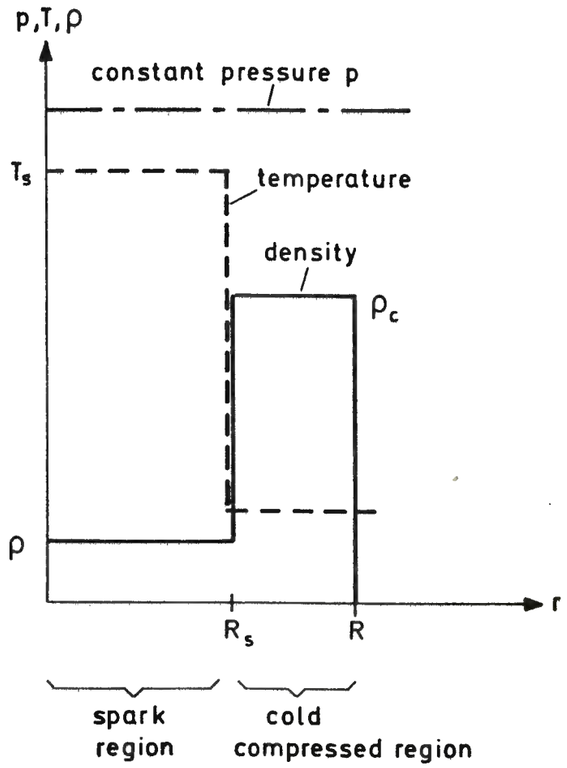

Fig. 1: Profiles of pressure p, temperature T, and density for the schematic ignition configuration

As an important modification of the Kidder-Bodner model, we assume constant pressure p over the total (hot and cold) fuel region. Kidder

and Bodner had assumed constant density implying a sharp pressure jump from the hot to the cold fuel region. However, typical implosion runs (see e.g. ref. 3 and section 3) show that the ignition point with maximum fuel ρR and maximum central temperature T_s is generally reached only after the shock, emerging from the centre after shell collapse, has passed through fuel and pusher. At this time, almost all the inward going kinetic energy has been converted to internal energy, and the pressure is nearly constant over the fuel. This is the realistic ignition situation. Replacing constant density by constant pressure leads to less optimistic gain curves than those discussed by Bodner. This is because now more energy goes into the compressed fuel part.

The model is defined by the following equations. The spark region is described as an ideal gas. Taking as ignition conditions

$$kT_s \geq 5\,keV \tag{1a}$$

$$H_s = \rho_s R_s \geq 0.4\ g/cm^2 \tag{1b}$$

one obtains for the density ρ_s, the radius R_s, the mass M_s, and the internal energy E_s of the spark

$$\rho_s = \frac{\mu_{DT}}{2kT_s} \cdot p \tag{2a}$$

$$R_s = H_s/\rho_s \tag{2b}$$

$$M_s = \frac{4\pi}{3} R_s^3 \rho_s \tag{2c}$$

$$E_s = 2 \cdot \frac{3}{2} kT_s \cdot \frac{M_s}{\mu_{DT}} \tag{2d}$$

Here, the atomic weight of DT $\mu_{DT} \cong 4 \times 10^{-24}$g, and p is the overall pressure.

The highly compressed region is described as a degenerate electron gas with the pressure

$$p = \alpha \cdot \frac{2}{5} n_e \varepsilon_F = 2.34 \cdot 10^{12} \cdot \alpha \rho_c^{5/3} \quad \text{(cgs units)} \qquad (3a)$$

and the internal energy

$$E_c = \alpha \cdot \frac{3}{5} \varepsilon_F \cdot \frac{M}{\mu_{DT}} = 3.50 \cdot 10^{12} \cdot \alpha M_c \rho_c^{2/3} \text{ (cgs units)} \qquad (3b)$$

The isentrope parameter α denotes the deviation from the completely degenerate expressions and labels different isentropes. Obviously, one has $\alpha \geq 1$. The Fermi energy is given by $\varepsilon_F = \hbar^2 (3\pi^2 n_e)^{2/3}/(2m_e)$ with the elctron mass m_e and the electron density $n_e = \rho_c/\mu_{DT}$ In the model, the density ρ_c of the highly compressed region is obtained from eq. (3a) and its mass M_c from eq. (3b). The total fuel energy $(E_s + E_c)$ is related to the input beam energy

$$E_{Beam} = (E_s + E_c)/\eta \qquad (4)$$

via the hydrodynamic efficiency η . The total fusion energy

$$E_{Fusion} = q_{DT} \cdot M \cdot \phi \qquad (5)$$

is given by the specific DT fusion energy $q_{DT} = 3.34 \times 10^{11}$ J/g, the total fuel mass $M = M_s + M_c$, and the burn rate

$$\phi = H_F / (H_o + H_F) \qquad (6)$$

with the burn parameter $H_o \cong 7$ g/cm^2, the total fuel (ρR)

$$H_F = \rho_s R_s + \rho_c (R - R_s) \qquad (7)$$

and the fuel radius $R^3 = 3M/(4\pi\rho_c) + (1 - \rho_s/\rho_c) R_s^3$. The value for H_o corresponds to a freely expanding DT sphere. In actual pellet implosions, pusher material tamps this expansion and increases the burn rate. On the other hand, asymmetry effects will degrade the burn so that the chosen H_o

may effectively describe a realistic situation. Finally, the pellet gain is given by

$$G = E_{Fusion} / E_{Beam}$$

Results for $G(E_{Beam})$ are shown in figs 2 -4. If the input energy is not sufficient for ignition

$$E_{Beam} < E_s^{ign}/\eta \qquad (8)$$

the model assumptions are $E_c = 0$, $M_c = 0$, $E_s = \eta E_{in}$, $M_s = E_s \mu_{DT}/ 3kT_s$, and $R_s = (3M_s/4\pi\rho_s)^{1/3} < H_s/\rho_s$. The break in the gain curves marks the point of ignition and the onset of propagating burn. The hydrodynamic efficiency η , the isentrope parameter α, and the central pressure p are chosen as free model parameters. A standard set obtained for these parameters from explicit code calculations in section 3 is

$$\eta = 0.05 \;,\; \alpha = 2 \;,\; p = 0.2 \text{ Tb} \qquad (9)$$

The gain curve for these standard parameters as well as neighbouring curves when varying η , α, and p are shown in figs. 2, 3, and 4, respectively. The standard curve has its ignition point at about 1 MJ. Changing the hydrodynamic efficiency from 5 % to 10 % in fig. 2, a gain band is obtained which almost reproduces the 'conservative' gain region predicted by the Livermore group.[4] Targets for heavy ion beam fusion have relatively low η and are located at the lower edge of this band. The gain is also lowered by going to higher cold fuel isentropes as seen from fig. 3; in the region of propagating burn one has $G \sim 1/\alpha$. High central pressures strongly decrease the ignition energy $E_{Beam}^{ign} \sim p^{-2}$, but are less important in the high gain regime. This is seen in fig. 4, where also lines of equal fuel mass are given. At high pressures, the ignition conditions can be achieved with exceedingly small masses. Such small targets may be an option for laser fusion, where sharp focussing and high beam power are possible. For heavy ion beam fusion, however, both these points are difficult to achieve. Therefore one is bound to take relatively large targets.

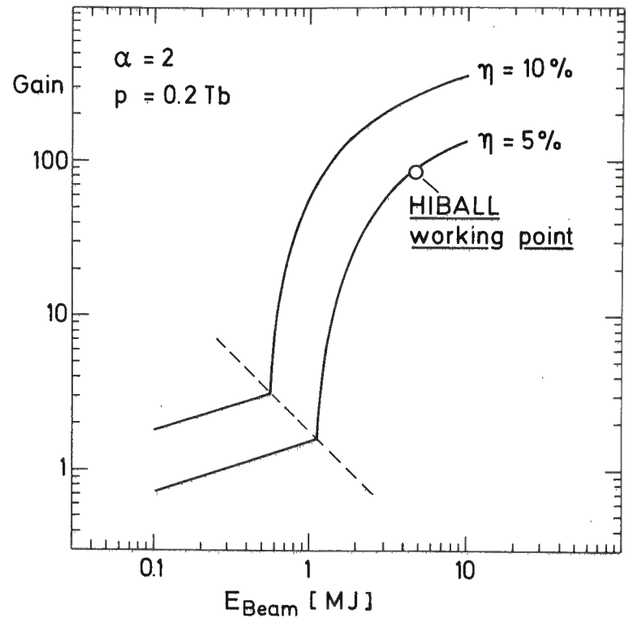

Fig. 2: Gain curves for different hydrodynamic efficiencies, α and p are kept fixed.

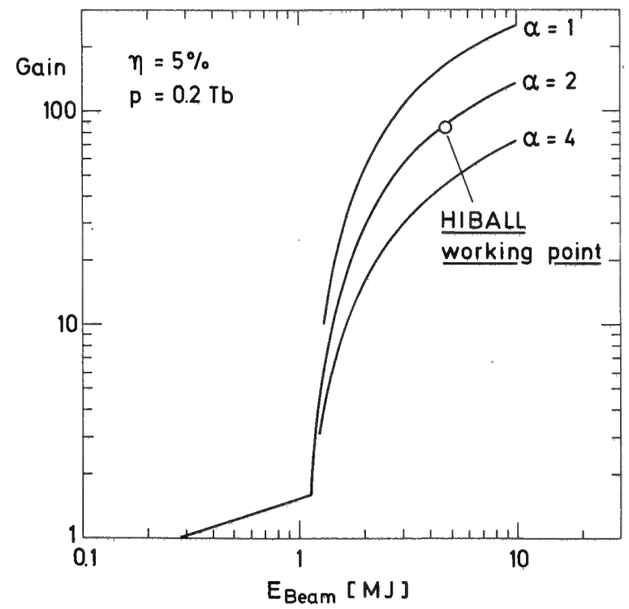

Fig. 3: Gain curves for different cold fuel isentropes, η and p are kept fixed.

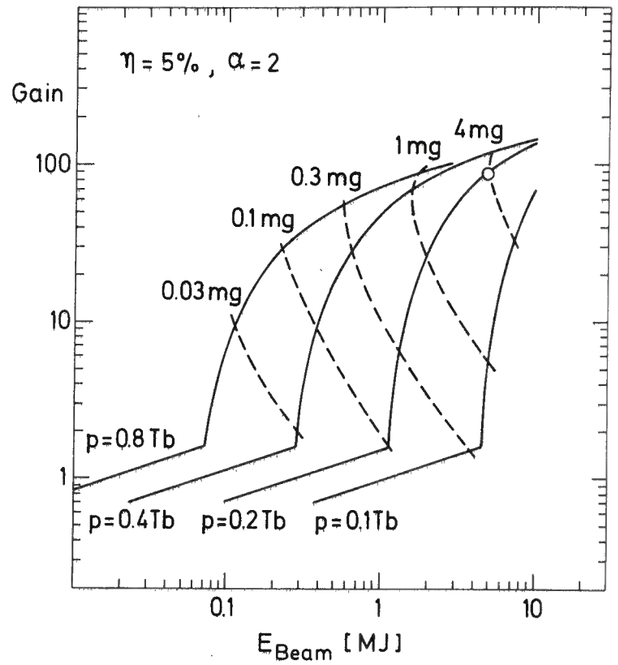

Fig. 4: Gain curves for different central pressures, η and α are kept fixed. The broken lines are curves of equal fuel mass.

The working point of the HIBALL reactor design has been chosen as

$$G = 83 \qquad (10)$$
$$E_{Beam} = 4.8 \text{ MJ}$$

which lies on the reference gain curve with the parameters (9). Within the model, one then finds the other pellet parameters as given in Table 1. The spark contains 2.5 % of the fuel mass, but 25 % of the fuel energy. Its density is less than one tenth of the compressed fuel density.

Table 1 HIBALL Pellet Parameters

total fuel	mass	M	= 4 mg
	confinement	(ρR)	= 3.4 g/cm^2
	burn rate	ϕ	= 30 %
	radius	R	= 124 µm
	pressure	p	= 0.2 Tb
	energy	E	= 240 kJ
spark	temperature	T_s	= 5 keV
	mass	M_s	= 0.1 mg
	confinement	$\rho_s R_s$	= 0.4 g/cm^2
	radius	R_s	= 77 µm
	density	ρ_s	= 52 g/cm^3
	energy	E_s	= 57 kJ
compressed fuel	density	ρ_c	= 630 g/ cm^3
	compression ratio	ρ_c/ρ_o	= 3000
	isentrope	α	= 2
	energy	E_c	= 183 kJ

In the next section, the stopping of heavy ions in hot dense matter is discussed, and stopping powers of Bi-ions are calculated for the absorber materials of the pellet described in section 3. The dynamic design parameters as pulse shape, maximum beam power, absorber pressure, implosion velocity etc. which are needed to achieve the ignition configuration are then discussed.

2. Heavy ion stopping powers in hot dense matter

2.1 General considerations

One of the advantages to use heavy ion beams for pellet fusion consists in the high stopping powers. The 10 GeV Bi-ions considered for HIBALL, e.g., are stopped in less than 0.5 mm of a Pb surface layer. So far, however, there exist no precise measurements for ion energies and target regimes of interest for pellet fusion. Stopping data in some cold target materials and for ion energies up to 5 MeV/nucleon have been measured recently at GSI.[5,6] In some cases, these data differ considerably from tables of Northcliffe and Schilling[7]. Tables extrapolated from the new data and covering the range of ion energies 2.5 - 100 MeV/nucleon and various projectile/target combinations have been published by Hubert et al.[8] No experimental information is available for stopping powers in hot dense matter. For pellet applications, one has therefore to rely on theoretical extrapolations.

Fortunately, there are good reasons to believe that classical stopping theory is applicable. As pointed out by Bangerter[9], the typical heavy ion beam for fusion (HIBALL values: 10 GeV Bi-ions, ion velocity $v_B/c \cong 0.3$, particle current at target $\approx$ 25 kA/cm^2) has an ion density of 10^{14} - 10^{15}/cm^3 as compared to a target electron density of $\approx 10^{23}$/cm^3. In this sense, it has to be considered as a dilute beam. The Debye screening length λ_D is 2 - 3 orders of magnitude smaller than the average ion seperation distance. One may therefore hope that anomalous collective effects can be ignored.

The dominant stopping mechanisms are then energy loss due to binary collisions with electrons at distances $r < \lambda_D$ and due to plasmon excitations at distances $r > \lambda_D$. For stopping in partially ionized plasma, it has been claimed that bound electrons at $r > \lambda_D$ do not contribute to the stopping power because of Debye screening[12, 13]. This is incorrect. It would have the consequence that stopping powers first decrease when a target is heated and increase only later at higher temperatures (> 50 eV) when the stopping contribution from the free electrons themselves becomes larger than their assumed screening

effect. However, a careful analysis of the energy flow at distances $r > \lambda_D$ (see e.g. Jackson's book[10]) shows that bound electrons in this region contribute to the energy loss just as the free electrons do. Therefore, as long as the ion velocity is large compared to the thermal velocity ($v_{el}^{th}/c \cong 0.003$ for T = 200 eV), the stopping power will monotonically increase with temperature. This is because the number of free electrons increases and energy is more easily transferred to free electrons than to bound ones. As an important result for ion pellet design it follows that ion ranges in cold material represent upper bounds and decrease when the target is heated.

2.2 The theoretical model for ion stopping

In this subsection, the basic equations for ion stopping in hot dense matter are given. The theoretical frame is kept as simple as possible. Standard stopping theory[10] is generalized and applied to partially ionized dense plasma. The topic has been discussed recently in detail by Mehlhorn[11] and others [12, 13]. The present work basically follows Mehlhorn's description except for a few points explained below.

The electronic stopping power for non-relativistic beams has the general form

$$S = -\frac{4\pi e^4 Z_B^{eff\,2} n_e}{m_e v_B^2} \ln\left(\frac{b_{max}}{b_{min}}\right) \qquad (11)$$

where e and m_e are charge and mass of the electron, Z_B^{eff} is the effective charge of the beam ion and v_B its velocity, $n_e = (\varrho_T Z_T)/(A_T m_p)$ is the electron density with the mass density ϱ_T, the charge number Z_T and the mass number A_T of the target atoms, and m_p is the proton mass. The minimum and maximum impact parameters are given by

$$b_{min} = Max\left\{\frac{Z_B^{eff} e^2}{m_e v_B^2}\,,\ \frac{\hbar}{m_e v_B}\right\}$$

$$b_{max} = \begin{cases} v_B/\bar{\omega} & \text{for bound electrons} \\ v_B/\omega_p & \text{for free electrons} \end{cases}$$

For the average ionization potential, we have used the expression

$$\hbar\bar{\omega} = 9\,eV * Z_T * (1 + 1.8/Z_T^{1/2}) * \exp\{2.7\,(Z_T^{ion}/Z_T)^2\}$$

which represents a fit to results of ref. 11. The plasma frequency of the free electrons, $\omega_p = (4\pi e^2 n_e Z_T^{ion}/m_e Z_T)^{1/2}$. Z^{ion} is the average ionization state of target atoms, and $\hbar$ Planck's constant. In the case of 10 GeV Bi-ions, the minimum impact parameter b_{min} is found to be equal to the Coulomb distance ($Z_B^{eff} e^2/m_e v^2$) over the whole stopping range implying that Bohr's classical stopping formula is valid. For most heavy ion applications, it is incorrect to use the quantum value $b_{min} = \hbar/(m_e v_B)$ which leads to Bethe's stopping formula. This point has been overlooked in a number of papers including Mehlhorn's[11]. Our choice for b_{max} takes into account binary collisions as well as plasmon excitations as discussed in the preceding section.

An important quantity is the effective charge Z_B^{eff} of the beam ion inside the stopping medium, since the stopping powers depend on $Z_B^{eff\,2}$. It is difficult to measure Z_B^{eff} directly, and it has therefore in general been determined indirectly from measured stopping powers on the basis of eq.(11). It is found that Z_B^{eff} is approximately a function of the ion velocity alone and independent of target properties. A good parametrization of existing data has been given by Nikolaev and Dmitriev[14] in the form

$$Z_B^{eff} = Z_B \cdot [1 + (Z_B^{\alpha} v_o/v)^{1/k}]^{-k} \qquad (12)$$

with the parameters $\alpha = 0.45$, $k = 0.6$, and $v_o = 3.6 \times 10^8$ cm/sec. We have used this formula taking for the relative velocity between beam ion and electrons $v = (v_B^2 + v_{el}^{th\,2})^{1/2}$ where $v_{el}^{th} = (2kT/me)^{1/2}$ is the thermal electron velocity and kT the temperature. The total stopping power is finally obtained by adding the contributions from bound and free electrons

$$\frac{dE}{dR} = \frac{1}{\varrho_T}\left(1 - \frac{Z_T^{ion}}{Z_T}\right) \cdot S_{bound} + \frac{Z_T^{ion}}{\varrho_T Z_T} G(v_B/v_{el}^{th}) \cdot S_{free} \qquad (13)$$

Here, the function $G(x) = (\mathrm{erf}(x) - 2 \times \exp(-x^2)/\sqrt{\pi})$ accounts for the temperature dependence of the Coulomb cross section in the case that the

thermal velocity v_{el}^{th} becomes comparable or larger than the ion velocity v_B. It is well known that the description given above breaks down for low ion energies. The Lindhard theory, applicable at low energies, gives for the bound electron contribution

$$S_{bound} = -k\sqrt{E_{ion}/A} \qquad (14)$$

In order to insure a correct treatment of the energy deposition near the end of the beam range, we have smoothly replaced expression (11) for S_{bound} by the Lindhard expression (14) at small energies, taking the parameter k from recent GSI measurements.[5] The calculated stopping power at small energies for Bi on solid lead is shown in fig. 5 together with GSI-data and values from the tables in ref. 8.

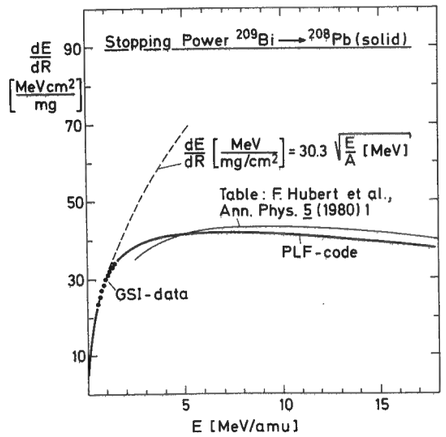

Fig. 5: Stopping powers of Bi on solid Pb at low energies.

2.3 Calculated ranges and stopping powers

As a central result of this study, ranges of Bi-ions on solid Pb, solid Li, and solid PbLi alloy as considered in the HIBALL pellet design are given in fig. 6 as a function of ion energy in the relevant energy region. The range of 10 GeV Bi on solid Pb is found to be

$$R(10\,GeV\ Bi \rightarrow Pb) \cong 0.30\ g/cm^2$$

in solid Li, it is

$$R(10\,GeV\ Bi \rightarrow Li) \cong 0.13\ g/cm^2$$

For stopping powers at finite temperature, the average ionization Z_T^{ion} of the target plasma has been calculated from the Saha equation using ionization energies derived within Thomas-Fermi approximation. As an example the ionization of Pb-plasma as a function of temperature and density is shown in fig. 7. Based on these results, deposition profiles of 10 GeV Bi-ions in different materials and at various temperatures relevant for pellet fusion have been calculated as shown in figs. 8 - 10. With increasing temperature, range shortening is found in all cases. The deposition profile in solid Pb is rather flat, and pronounced Bragg peaks only develop at higher temperatures. In a light material like Li, the average stopping is higher than in Pb and the effect of range shortening saturates at a temperature of about 100 eV as seen in fig. 9. At this temperature, the material is fully ionized.

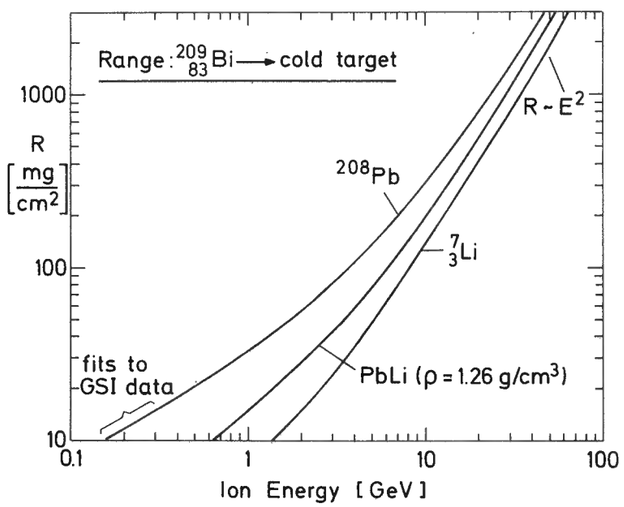

Fig. 6: Ranges of Bi-ions in different solid materials as a function of ion energy

In fig. 10, deposition profiles are shown for the HIBALL pellet. The beam first passes through a heavy Pb layer with relatively low stopping power. This layer serves as a tamper. The rest of the beam energy (almost 50 %) is then absorbed in a PbLi layer with low density and high stopping power. It is heated to higher temperatures than the Pb layer. For simplicity, constant temperatures are chosen in fig. 10 for each layer. They correspond to typical values of the implosion calculation discussed in the next section. It should be noted that deposition profiles of light ion beams show a much more pronounced Bragg peak than the heavy ion beams discussed here. Light ion beams are therefore more suited to create an implision configuration with a heavy cold tamper outside and a light hot absorber inside which pushes the fuel with high efficiency. The advantage of this design is somewhat reduced when used for heavy ion beam fusion as in the present study.

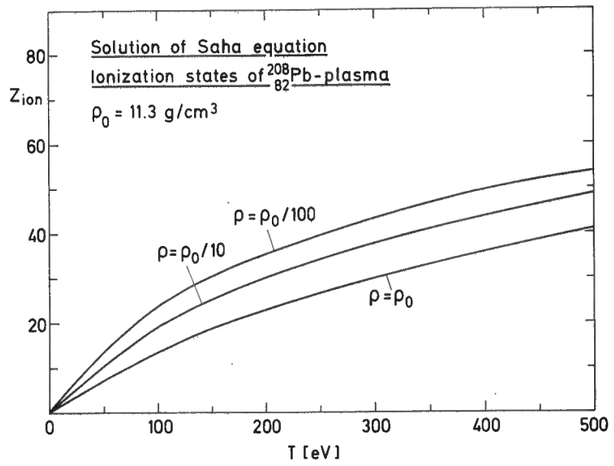

Fig. 7: Average ionization of Pb-plasma as a function of temperature and density

A further degradation of coupling efficiency between beam and implosion dynamics is due to the fact that, in a realistic situation, the beam arrives at the pellet surface not perfectly focussed (see e.g. ref. 15) The effect of defocussing has been studied in ref. 16. It tends to wash out any Bragg peak in the deposition profile. Since the exact beam properties at target are still uncertain, we have chosen box deposition profiles with constant dE/dR in the following implosion calculation.

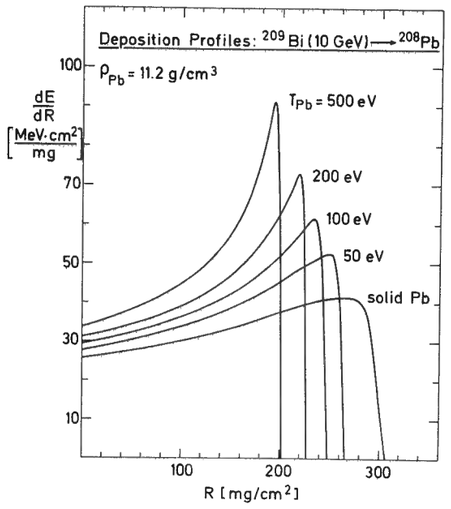

Fig. 8:
Stopping power as a function of range for Bi on Pb for different target temperatures

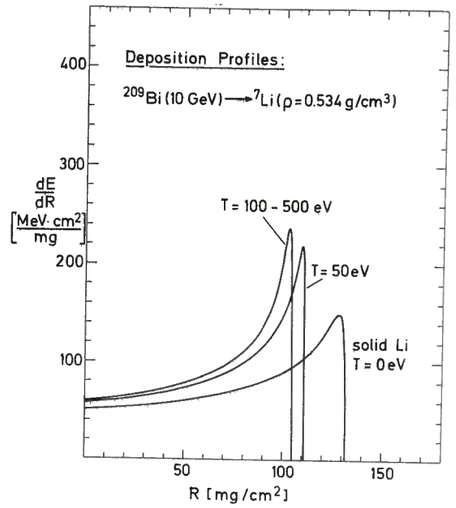

Fig. 9:
Same as fig. 8, but for Bi on Li

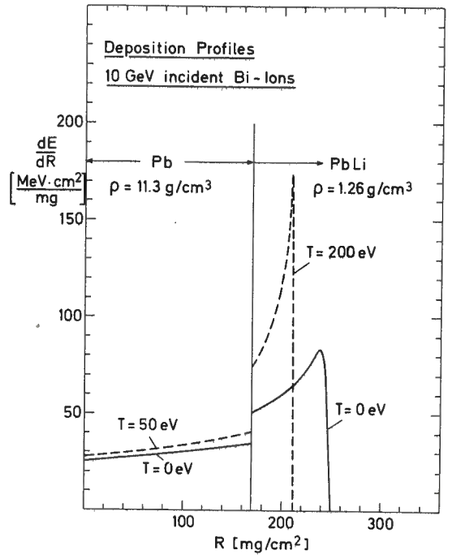

Fig. 10:
Energy deposition of 10-GeV Bi-ions in the absorption layers of the HIBALL pellet. Solid line for cold target, broken line for typical temperatures during implosion

3. A specific pellet design

3.1 General consideration

In this section, a single shell pellet design is considered, and the results of an implosion calculation are presented in detail. The intention is to provide insight into the dynamics of a heavy ion induced pellet implosion, to check the consistency of the general HIBALL parameters with the requirements of the pellet and to discover critical points. The results indicate that the beam parameters assumed so far are not consistent. Most critical points are ignition and symmetry. The assumed power of 240 TW is too low to insure a stable and igniting implosion, at least for the envisioned single shell design. The presented calculation achieves ignition with 240 TW, but only at the price of a highly optimized pulse shape, a thin pusher (6 mg) and a reduced amount of fuel (2 mg). The required output energy of 400 MJ is obtained due to a high burn rate. However, a rough estimate then shows that the implosion symmetry will be destroyed due to Rayleigh-Taylor (RT) instability. A thicker pusher that survives RT-instability is needed as well as 4 mg fuel to allow for a more realistic burn rate. This will require considerably more beam power for ignition, probably in the order of 500 TW. An alternative approach may be a double shell pellet design which has been found to require less power for ignition due to a central igniter[17].

It should be kept in mind that the present calculations are based on a simple hydrodynamic code (see description below) and are subject to large uncertainties on top of those inherent to pellet design in general. A particular problem not further addressed in the following is related to asymmetric irradiation of the pellet in the HIBALL reactor. Due to high density and relatively low temperature in the beam deposition region, lateral heat conduction will be rather ineffective to smooth out these asymmetries, at least in the present design.

3.2 The pellet configuration

The pellet considered in this work closely follows a design proposed by Bangerter and Meeker[18] for light ion beam fusion. A perspective view is given in fig. 11. The pellet consists of a spherical hollow shell made of three layers as shown in fig. 12. The cryogenic fuel is contained in the inner layer, the outer layers are made of low density PbLi alloy and high density Pb. They serve as pusher/absorber and tamper, respectively. The PbLi-alloy replaces the TaCOH material of the Bangerter-Meeker design and has been chosen for reasons of chemical compatibility with the environment in the HIBALL reactor cavity. The main reason for choosing a low density layer in the middle is to have a low density pusher in order to prevent RT-instability at the pusher-fuel interface during the final stage of implosion. The other advantage in having a heavy tamper outside and a light absorber material inside is related to beam target coupling and has already been discussed in the section 2.3.

The masses of the Pb and PbLi layer have been determined such that the interface between these layers is approximately stationary during the implosion and, secondly, by the requirement that beam ions have stopped in the cold absorber 80 μm before reaching the fuel. This inner region of the PbLi layer is not directly heated by the beam and forms the pusher. The pusher mass (6 mg) as the well as fuel mass (2 mg) have been chosen such that ignition is achieved at a beam power of 240 TW (compare discussion in section 3.1). The outer radius of the pellet has been fixed to 3 mm. This is a minimum value set by the requirements of final beam focussing.

3.3 The pellet code MINIHY

The 1D-Lagrangian hydrodynamic code MINIHY used for the implosion calculation is characterized by the following physical features:

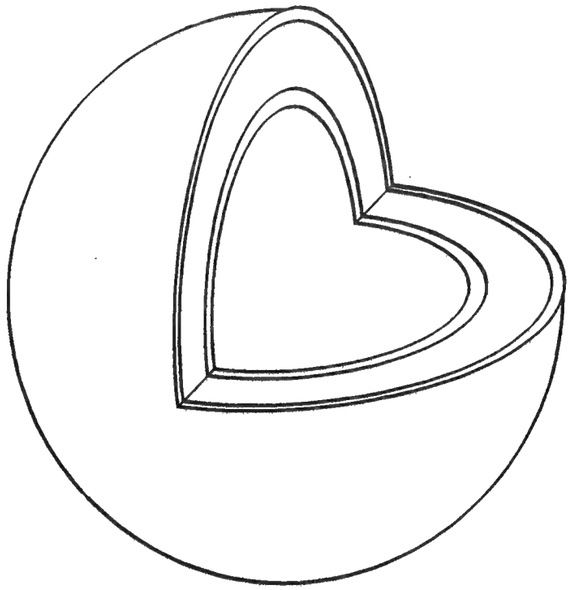

Fig. 11: Perspective view of the HIBALL pellet

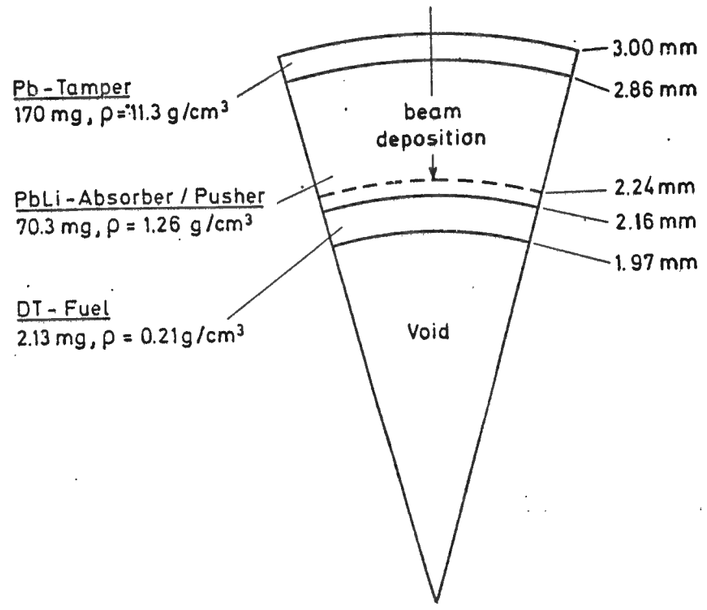

Fig. 12: Sector of the HIBALL pellet

A. One temperature for electrons and ions

It has been checked that this is sufficient for ion beam driven implosions[19], since energy deposition occurs in dense material and temperatures are typically below 500 eV. This is different from the situation in laser fusion where electron and ion temperatures decouple in the corona.

B. Spitzer thermal conductivity, no flux limit

This is sufficient for the same reasons as mentioned under point A.

C. DT burn with local α deposition and free neutron escape

Since this treatment may overestimate ignition, fusion processes are switched on only when the central temperature reaches 5.6 keV. At this temperature, fusion energy production overtakes losses by bremsstrahlung. Fuel depletion is accounted for during burn.

D. Ideal gas equation of state allowing for electron degeneracy

A crucial point is that the Fermi temperature which controls the transition to the degenerate state is not calculated from the total electron density n_e in the medium (as e.g. in the original version of the Medusa code[20]), but from an effective density of unbound electrons n_e^* which is determined by an ad hoc description of pressure ionization in the form

$$n_e^* = n_e * \exp\{-1/(V_0 n_e)\}$$

for DT, where $V_0 = 4\pi/3 * (\hbar^2/m_e e^2)^3$ is the volume occupied by a bound electron, and for heavier materials in the form

$$n_e^* = \begin{cases} n_e \cdot [1 - \exp(-(\varrho-\varrho_0)/(\beta\varrho_0))] & \text{for } \varrho > \varrho_0 \\ 0 & \text{for } \varrho \leq \varrho_0 \end{cases}$$

where ϱ_0 is the solid density and β an adjustable parameter. In the present calculation, $\beta = 200$ has been chosen for Pb, and $\beta = 50$ for PbLi. To be definite, the isotherms for DT and Pb in the (p, ϱ) plane have been plotted in figs. 13a and 13b. They show at least qualitatively a reasonable behaviour, in particular near the limiting degeneracy curve which is most important for a correct description of the high compression regions in the implosion.

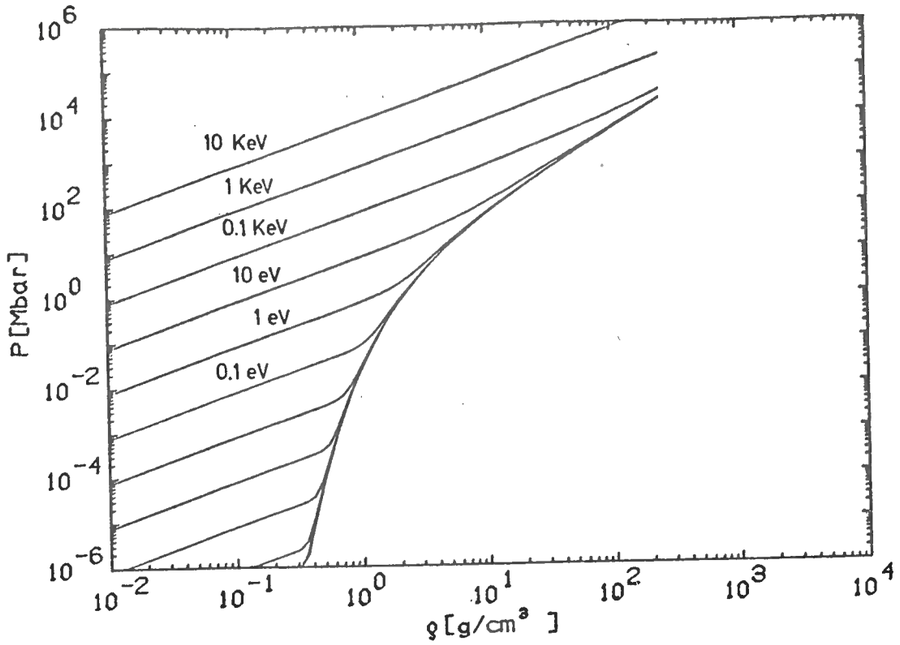

Fig. 13a: Equation of state for DT used in the calculation

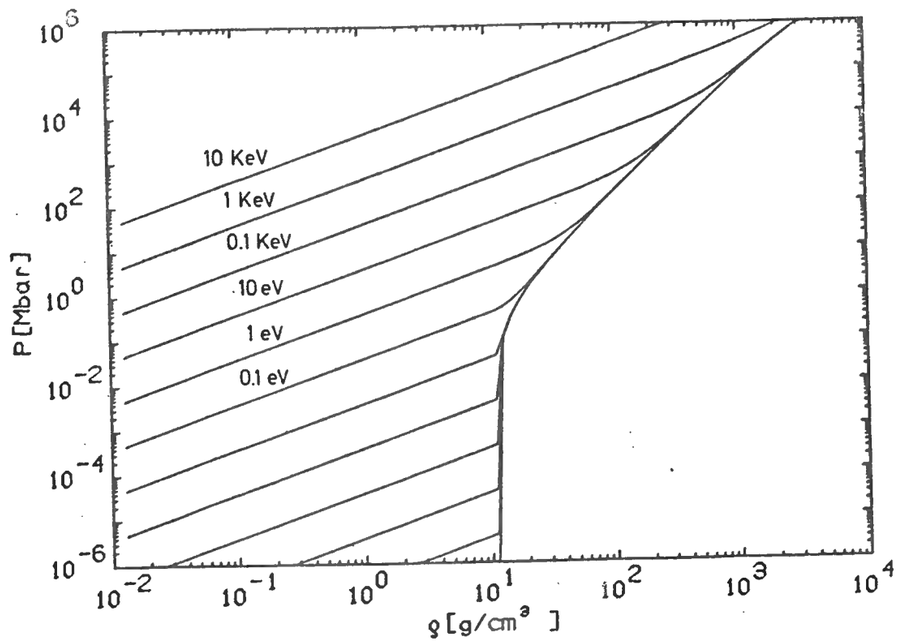

Fig. 13b: Same as fig. 13a, but for Pb

With a more realistic equation of state, one would have to deposit more energy to create the same driving pressure in the absorber. Also, absorber temperatures would be higher at the same pressures. A critical point will be radiation transport which has not been included in the code, so far. The high-Z Pb layer is optically thick, and radiation losses through the surface may be estimated by black body radiation. For the proposed pellet design, one finds a loss of 6 kJ for 50 eV surface temperature, 100 kJ for 100 eV, and 1.6 MJ for 200 eV. These are upper limits, but they demonstrate that a careful treatment of radiation as well as a more realistic equation of state are needed in the future development of this work. Nevertheless, no dramatic changes are expected for the overall implosion results. Concerning the beam energy deposition, it has been assumed $dE/\varrho\, dx$ = const (see discussion in section 2.3). The implosion calculation has been performed on a Lagrangian mesh with 100 zones (36 for DT) and with progressively finer zoning towards the inner interface of each layer.

3.4 The pellet implosion

3.4.1 The general view

The optimized pulse shape to implode the described pellet configuration and to drive it to ignition is displayed in fig. 14. It consists of a 20 nsec prepulse at a power level of 2.4 TW and a 10 nsec main pulse at 240 TW with a 2 nsec rise time in between. The pulse is cut of at 32 nsec, since a further continuation would not improve the implosion result. The total pulse energy is 2.7 MJ. The corresponding r-t-diagram of the imploding shell is shown in fig. 15. The solid lines describe the motion of the outer pellet surface, the interfaces between the Pb, PbLi, and DT layer, and the inner DT surface, respectively. The broken lines display the temperature evolution in the deposition region. Ignition and burn occurs at about 37.7 nsec near R = 0.

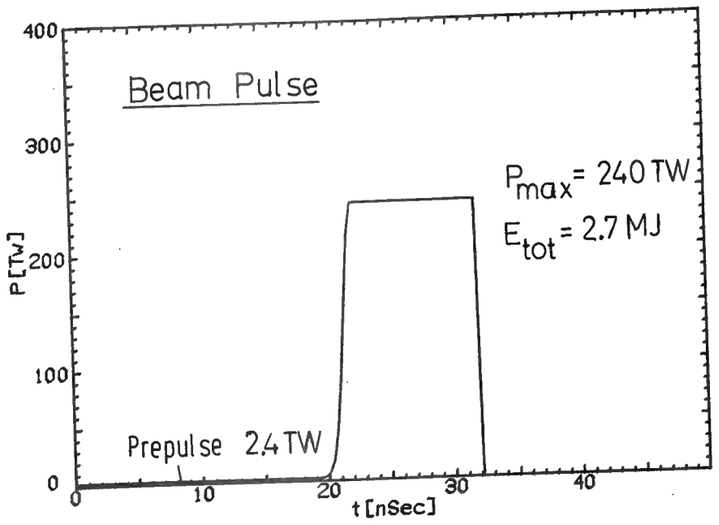

Fig. 14: Pulse shape of the HIBALL design

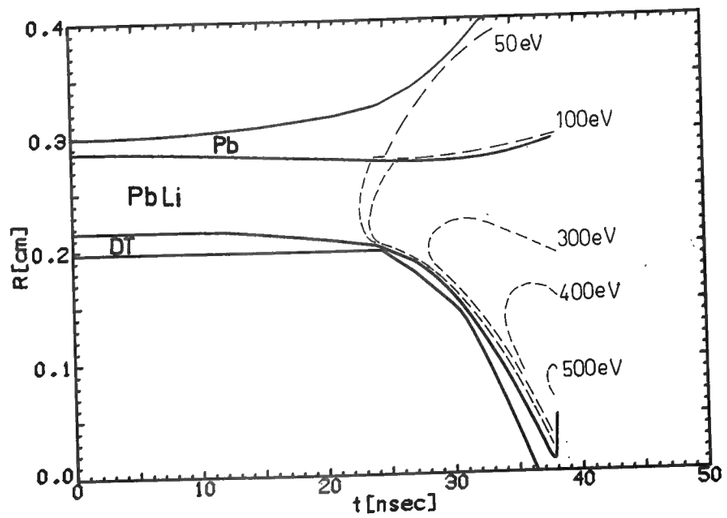

Fig. 15: Implosion of the HIBALL pellet driven by pulse shown in fig. 14

The ion driven implosion looks rather different from that driven by a laser. It is essentially the explosion of a massive metal shell pushing the fuel at its inner front. The 10 GeV Bi-ions pass through 97.5 % of the shell's mass and deposit their energy deeply inside the volume, whereas laser deposition occurs far outside in a low density corona and the imploding material is driven by an ablating surface. As a consequence, the temperatures in the ion deposition region remain rather low (< 500 eV) as compared to corona temperatures in laser fusion, and no problem with hot electrons is expected to occur. A disadvantage of the low temperatures is that heat conduction is slow and therefore ineffective to smooth out irregularities due to asymmetric irradiation of the pellet.

3.4.2 Absorber, pusher, and fuel during implosion

It is instructive to look at the profiles of temperature Θ, density ϱ, and pressure p given in figs. 16a-j for different times in conjunction with the r-t-diagram. Fig. 16a shows the unperturbed pellet. The solid points in the broken line for the density mark the interfaces. The profiles at 18 nsec are seen in fig. 16b. The prepulse has heated the absorber to about 5 eV, the tamper interface stands like a rigid wall, the heated PbLi is flowing inwards, and a sharp density and temperature jump has built up at the border to the unheated PbLi which now forms the pusher. The steep gradients at this interface, formed at early times, stay on through all stages of the implosion. It is subject to severe RT-instability, a point further discussed in section 3.4.5. At 18 nsec, the first shock generated by the prepulse has just entered into the unperturbed fuel. At 24.5 nsec, it has almost reached the inner surface of the fuel closely followed by the second strong shock launched by the main pulse which was switched on at 21 nsec. This is seen from figs. 16c and 16d. The importance of these two shocks and their relative timing for forming the ignition spark will be discussed in section 3.4.6. Here, one should again pay attention to the r-t-diagram (fig. 15) and to the way the inner fuel surface is set into sudden fast motion upon arrival of the shocks. It then travels at almost constant speed

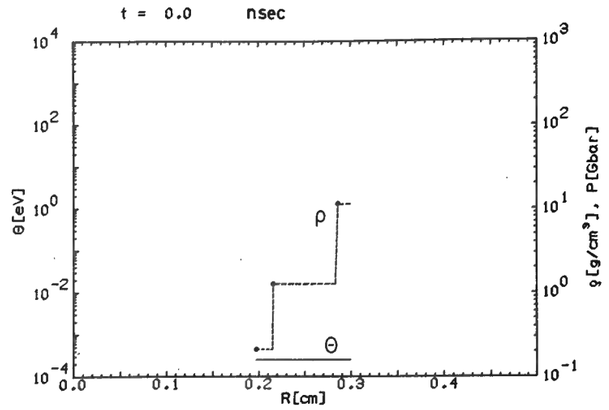

Fig. 16a: Distribution of density ρ , temperature Θ , and pressure p in the pellet at time t = 0. The solid points in the density line mark the interfaces. The pressure is still too low to be seen at this time.

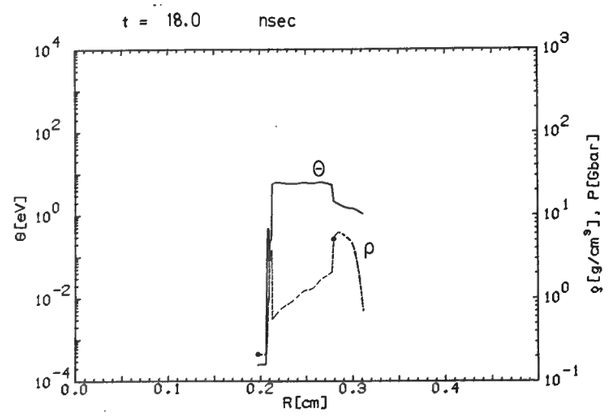

Fig. 16b: Distributions at t = 18.0 nsec.

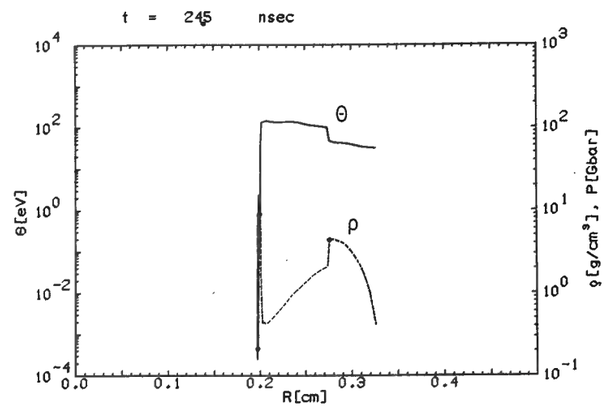

Fig. 16c: Distributions at t = 24.5 nsec.

until the accelerated pusher catches up at about 31 nsec and gives the fuel another kick involving the passage of a third shock through the fuel. This fuel bouncing has been described before by Kidder[3]. It is also important for ignition.

At 36.40 nsec, the inner surface arrives at the centre (void closure). The fuel has now an average velocity of 2.5 x 10^7 cm/sec. Its kinetic energy amounts to 2.3 % of the input beam energy, whereas its internal energy is only 0.2 %, at this moment. The profiles are plotted in fig. 16e. A remarkable feature is the temperature distribution in the fuel which steeply rises towards the centre and is forming the ignition region. The pressure has now increased to more than 100 Mbar in the central region and appears on the scale chosen in the diagrams. Typical pressures in the absorber at main pulse time range between 10 and 100 Mbar.

3.4.3 Ignition and burn

Ignition (defined here as time when the central temperature reaches 5.6 keV) occurs at 37.647 nsec, about 1.2 nsec after void closure. During this time, a strong reflected shock has traveled outwards through the fuel and is clearly seen in the pressure profile of figs. 16f and 16g at a position of 120 µm. (Note that a von Neumann viscosity is used in the hydrodynamic code, and shocks do not appear as sharp discontinuities, but smeared out over several Lagrangian cells). The return shock has finally brought the fuel into the ignition configuration. In fig. 16g, one should notice

(a) the constant pressure over the fuel of $p \cong 0.17$ Tbar,

(b) the spark region extending to 70 µm with a temperature near 5 keV, a density around 50 g/cm^3 and $(\rho R)_{spark}$ 0.4 g/cm^2,

(c) the highly compressed fuel region extending from 70 µm to 105 µm with a density plateau at 600 g/cm^3 and a temperature around 150 eV; the total fuel $\rho R \cong 2.3$ g/cm^2.

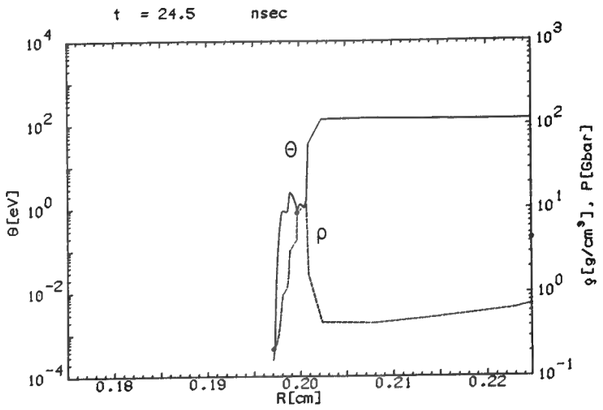

Fig. 16d: Enlarged view of fig. 16c. First two shocks are seen in fuel

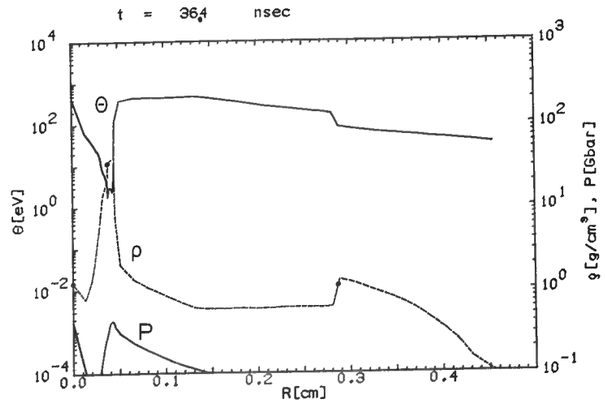

Fig. 16e: Distributions at void closure time t = 36.4 nsec. Region of high fuel temperature seen in the centre.

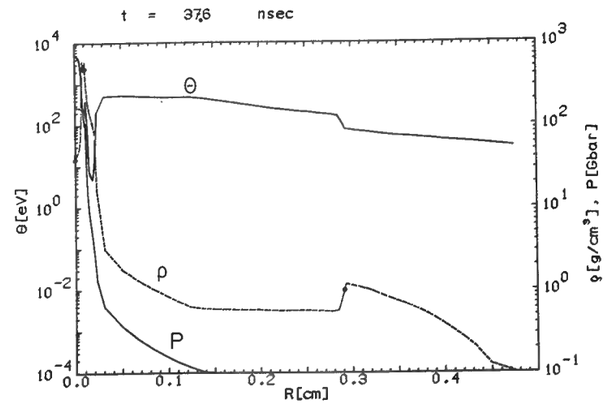

Fig. 16f: Distributions at ignition time t = 37.6 nsec.

These values are very near to those of the HIBALL working point which have been determined within the simple gain model of section 1 and have been listed in table 1. The present calculation shows that the ignition configuration postulated there can actually be achieved dynamically. In particular, it confirms the key assumption of constant fuel pressure in which our model differs from that of Kidder and Bodner.

At ignition time, the fuel has come almost to rest. The fuel kinetic energy now amounts to 0.07 % of the total input energy, but the internal energy has increased to 4.2 % or 113 kJ. At the same time, there still exists 4.5 % of the energy in form of inward going kinetic energy, mainly located in the massive pusher. The bulk of the energy occurs as internal energy of PbLi ($\approx$ 43 %) and as energy of the tamper (18 % internal, 30 % kinetic). The absorber/tamper interface has hardly moved during the implosion, but about half of the beam energy has been deposited in the tamper and Pb is strongly flowing outwards at this time.

After ignition, it takes roughly 200 psec until burn has spread into the dense fuel region, and fusion energy is released in a short burst of about 20 psec. Fig. 16h displays the situation shortly after burn. The central temperature is now above 10 keV, the burned up fuel is expanding, the outgoing burn shock sits at 0.6 mm, but has been left far behind by a fast moving heat wave with the front located at 1.5 mm. The calculated gain is 212, corresponding to a burn rate of 80 %. Such a high burn rate is probably unrealistic and expected to be degraded by effects (e.g. nonsymmetric implosion) not simulated in our code. In the present calculation, it is explained by the strongly tamping effect of the pusher ($(\varrho R)_{Pusher} \approx 3$ g/cm^2) and its high, inwards directed kinetic energy during burn time.

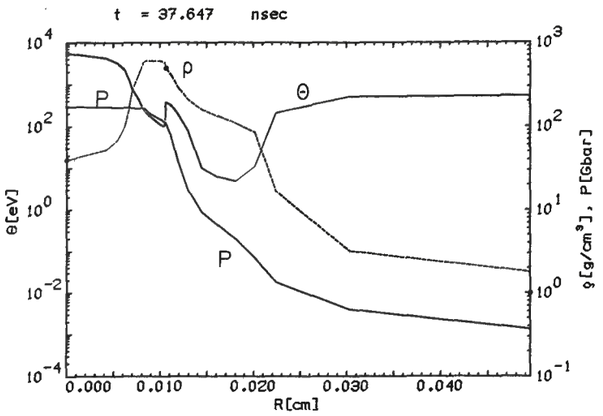

Fig. 16g: Enlarged view of fig. 16f. The ignition configuration with constant pressure over the fuel is seen for R ≈ 110 µm.

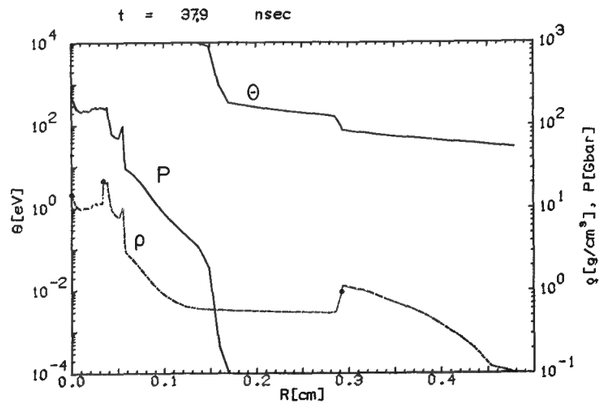

Fig. 16h: Distribution after burn at t = 37.9 nsec. A heat wave at 0.15 cm is seen travelling to the right far ahead of the burn shock wave at 0.06 cm.

3.4.4 Pulse shape, shocks, ignition

The formation of the ignition spark and how it is related to the pulse shape is now discussed in some more detail. The problem is to drive a certain inner part of the fuel to a much higher isentrope than the rest of the fuel, the entropy of which should be kept as low as possible. In pure gas dynamics, which are approximately valid for the imploding fuel, the entropy of a fluid element is a constant of motion as long as no shock passes through. The amount of entropy increase due to a shock depends on its strength in a non-linear way. The concept followed in the present design work to achieve an optimal ignition configuration is schematically outlined below and then illustrated by showing the fuel entropy evolution in the code calculation. It involves a sequence of 4 shocks passing through the fuel.

I. Prepulse shock

The prepulse (few TW) launches a 1. shock S1 which homogeneously heats the cryogenic fuel to a temperature of about 0.5 eV.

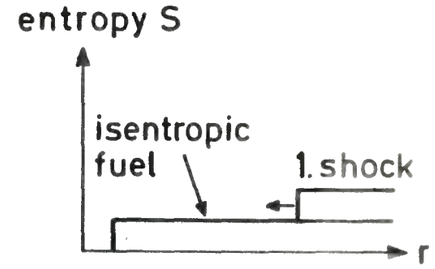

II. Main pulse shock

The main pulse (some 100 TW) launches a second shock S2 into the fuel which is timed to overtake S1 near the inner fuel surface.

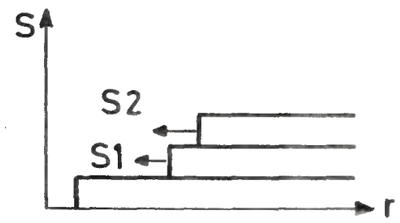

The combined shock S12 is much stronger than the sum of the original shocks and produces a region of higher entropy.

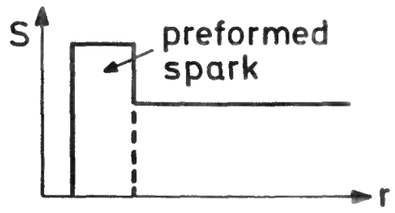

III. The bounce shock

The bounce shock (see section 3.4.2) passes through a sloping density profile near the inner fuel surface and adds selectively entropy to this region.

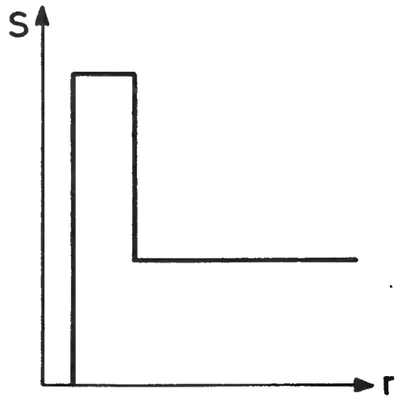

IV. The return shock

The return shock from central collapse finally shapes the spark and brings it to ignition temperature.

In fig. 17, it is shown to which extent this schematic ignition concept works in the actual code calculation. The ratio $(p/\varrho^{5/3})$ normalized to its value for a degenerate electron gas has been chosen as an approximate measure for the entropy and has been plotted over the fluid cells of the Lagrangian mesh for different stages of the implosion. Cell 1 is located at the inner surface of the fuel, cell 36 at the interface with the pusher. For 24 nsec, one observes the first two shocks S1 and S2 as jumps in the entropy distribution (compare the corresponding density jumps in fig. 16d). At 27 nsec, both shocks have passed the fuel. The timing has been such that S2 has caught up with S1 at Lagrange cell 6, and then the combined shock S12 has propagated further to the left and has generated a region of increased entropy over the last few cells. The preformed spark is clearly seen in the 27 nsec curve. The next increase in entropy is due to the third shock created by fuel bouncing. At 31 nsec, it has already passed the fuel, but the entropy curve at this time shows what has happened. In propagating through the fuel to the left, the bounce shock has met at Lagrange cell 16 with a rarefaction wave

running to the right. This has caused the sharp entropy increase towards the inner surface. Finally, at 37.65 nsec, after passage of the return shock, the $p/\varrho^{5/3}$ curve for the ignition configuration (compare fig. 16g) is obtained. Its lower part corresponds to the highly compressed, electron degenerate fuel. Notice that this part cannot be directly compared with the other curves of the plot due to the electron degeneracy. Entropy is calculated differently in this case. This becomes clear from the broken curve labelled by $\alpha = 1$ which represents the lowest isentrope possible for the degenerate gas. However, it is interesting that the degenerate branch lies very close to the optimal isentrope $\alpha = 1$. This is indeed an optimal run. Not withstanding the 4 shocks which have gone through the fuel, the overall compression has been almost adiabatic. The $p/\varrho^{5/3}$ distribution assumed in the gain model of section 1 for the HIBALL pellet is given in fig. 17 by the broken line $\alpha = 2$, including the spark region at the left with a much higher isentrope. It compares well with the code run.

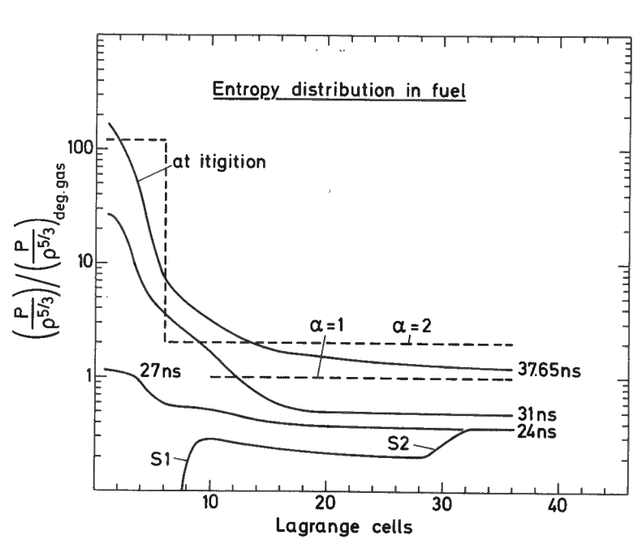

Fig. 17: Time evolution of $(p/\varrho^{5/3})$ distribution in fuel

It is concluded that the idealized ignition configuration assumed by the gain model can approximately be obtained by implosions with optimized pulse shape. With the ignition concept described above, size and form of

the spark is mainly determined by the timing of the first 2 shocks which is related to the length of the prepulse and to the power of prepulse and main pulse. The exact values to be chosen also depend on the actual pellet configuration. One problem has been to make the second shock strong enough for reaching final ignition. It has been solved by taking a short rise time of the main pulse. A general experience with these heavy reactor targets is that it is easy, at least in 1D-calculations, to obtain high compression in terms of (ϱR), but it is difficult to achieve high enough temperaturs in the centre. The ignition requirement sets the lower bound for the beam power. Certainly more power than 240 TW is needed to make the present design less sensitive to the pulse shape.

3.4.5 Estimated growth of Rayleigh-Taylor instability

Symmetry is an even more critical point than ignition. A rough estimate shows that the present design fails due to RT-instability. The pusher region is probably not thick enough to survive this fluid instability. Since no 2-dimensional code was available to follow the evolution of the instability in detail, the growth rate has been estimated by applying linear RT-theory for an incompressible fluid. The ingredients for our analysis are given in fig. 18. The upper plot shows the evolution of pusher thickness with time. It is seen that the pusher is strongly compressed during implosion and has a thickness $d_{min} \cong 15$ µm at the time of maximum acceleration which amounts to $g \cong 2 \times 10^{15}$ cm/sec^2 as seen from the velocity plot in fig. 18. The pusher is subject to RT-instability, since it has high density and is accelerated by low density absorber material. The density gradient at the interface is very steep (compare figs. 16b-e), and the Atwood number is $\cong 1$. We have chosen $k_{crit} \cong \pi / d_{min}$ for the wave number of the most critical mode. The exponential growth rate

$$\sigma = (\pi g / d_{min})^{1/2}$$

then leads to an estimated growth factor

$$\exp\{\sigma \cdot \Delta t\} \cong 10^9$$

taking as the relevant implosion time $\Delta t \cong 10$ nsec. Such a growth rate will certainly destroy the symmetry of the pusher during implosion and will prevent burn. According to the simple analysis, a pusher 4 times as thick would lead to a growth factor of $\approx 10^5$ which might be tolerable.[21] It may be that these formulas of linear RT-theory overestimate the growth of the instability and that non-linear effects (see e.g. ref. 22) not taken into account here improve the situation. But there is little doubt that symmetry is a most critical issue in this design. A more massive pusher may help, although it will be compressed to higher densities and the thickness at maximum acceleration will not increase linearly with mass. Also, a more massive pusher will require more beam power for implosion. The symmetry problem has to be studied in much more detail including the question of initial perturbations and irradiation asymmetry.

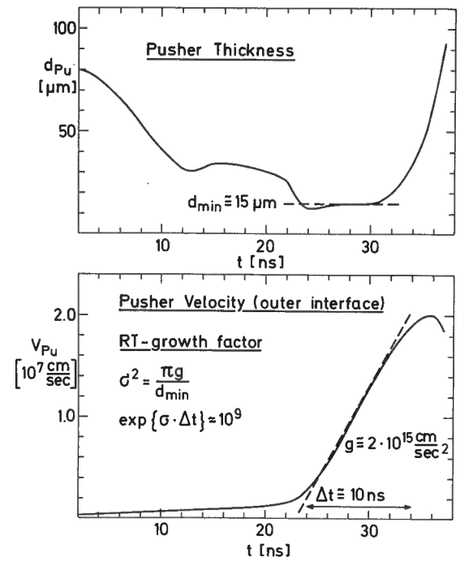

Fig. 18: Pusher thickness and velocity of the pusher/fuel interface as a function of time.

4. Conclusion

A pellet design for heavy ion beam fusion has been presented displaying the different stages of implosion and describing the physical mechanisms such as beam deposition, the relation between pulse shape, shock evolution and ignition, and also pusher dynamics and implosion symmetry. An elementary version of heavy ion stopping theory has been outlined, studying in particular the temperature dependence of stopping powers and ranges. In addition, a gain model has been developed which is based on the results of the explicit design and allows for scaling of various parameters. It produces gain curves similar to those obtained by the Livermore group and provides a physical interpretation. The model differs from that of Kidder and Bodner in the assumption of constant pressure over the fuel at ignition.

With respect to HIBALL, the gain model yields the HIBALL working point with a gain of 83 at an input energy of 4.8 MJ in a natural way. It corresponds to a hydrodynamic efficiency of 5 % and a compressed fuel isentrope of $\alpha = 2$ in close agreement with the explicit design. Concerning the beam power, however, the code calculation indicates that 240 TW, assumed for HIBALL so far, are insufficient to insure a stable and igniting implosion. The present design achieves ignition at 240 TW only with a highly optimized pulse and will not survive RT-instability. It requires more beam power to improve on both points. Also, consideration of a more realistic equation of state and of radiation losses will increase the requirements on beam power, probably to a level of 500 TW. A final remark should be made with respect to the pulse shape. It has turned out that a carefully timed prepulse is important for effective ignition and should be taken into account in the general HIBALL design.

References

1. S. Bodner, NRL Memorandum Report 4453 (1981).

2. R.E. Kidder, Nucl. Fus. 16 (1976) 405.

3. R.E. Kidder, Nucl. Fus. 19 (1979) 223.

4. J.H. Nuckolls, in LLL Laser Program Annual Report 1979, vol. 2, p. 3-2.

5. H. Geissel, T. Kitahara, Y. Laichter, and P. Armbruster, 'Stopping powers of 0.2-1.4 MeV/u heavy ions in solids', preprint GSI Darmstadt (1980).

6. R. Bimbot, D. Gardes, H. Geissel, T. Kitahara, P. Armbruster, A. Fleury, F. Hubert, Nucl. Instr. Meth. 174 (1980) 231.

7. L.C. Northcliffe and R.F. Schilling, Nuclear Data Tables A7 (1970) 233.

8. F. Hubert, A. Fleury, R. Bimbot, D. Gardes, Ann. Phys. (Fr.) 5 (1980) 1.

9. R.O. Bangerter, Proc. Heavy Ion Fusion Workshop, Report ANL-79-41, p. 415 (1979).

10. D. Jackson, 'Classical Electrodynamics'

11. T.A. Mehlhorn, Report Sand 80-0038 (1980).

12. K.A. Brueckner and N. Metzler, 'Stopping power for energetic ions in solids and plasmas', preprint UCSD (1980).

13. J.E. Rogerson, NRL Memorandum Report 4485 (1981).

14. V.S. Nikolaev and I.S. Dmitriev, Phys. Lett. 28A (1968) 277.

15. K.A. Brueckner, N. Metzler, and R. Janda, Phys. Fluids 24 (1981) 964.

16. K.A. Brueckner and N. Metzler, 'Targets for heavy ion fusion', preprint UCSD (1980).

17. J.D. Lindl and R.O. Bangerter, Report UCRL (1980).

18. R.O. Bangerter and D.J. Meeker, Report UCRL 78474 (1976).

19. S. Jorna, N. Metzler, and P. Hammerling, Phys. Lett. 80A (1980) 308.

20. J.P. Christiansen, D.E.T.F. Ashby, and K.V. Roberts, Comp. Phys. Commun. 7 (1974) 271.

21. R.O. Bangerter, J.D. Lindl, C.E. Max, and W.C. Mead, Report UCRL 77 048 (1975).

22. Ril. McCrory, L. Montierth, R.L. Morse, C.P. Verdon, Phys. Lett. 46 (1981) 336.